Journal of Marine Research, 71, 227–252, 2013

Instability of a tidal mixing front in the presence of realistic tides and mixing

by K.H. Brink[1,2]

ABSTRACT

Instability and lateral eddy fluxes associated with a tidal mixing front are studied using idealized primitive equation numerical model runs. The front itself develops as a result of turbulence associated with imposed tidal currents over a sloping bottom. Thus, the model includes realistic levels of turbulence and time-dependence in the base-state conditions. In all of the 21 configurations considered, the front is unstable to fluctuations that usually draw energy primarily from the potential energy pool. Scalings are developed to parameterize a) the location of the tidal mixing front; b) the eddy kinetic energy; and c) the lateral eddy coefficients. In all cases, baroclinic instability enhances the lateral mixing relative to the two-dimensional case, but the extent of enhancement varies with the input parameters. Preliminary model runs that include a simple nutrient-phytoplankton-zooplankton-detritus biological model do not suggest any substantial ecological effect of the baroclinic instabilities. The lack of a strong biological effect, despite the enhanced eddy transports, occurs because of the near cancelation of oppositely directed cross-isobath eddy fluxes in the upper and lower parts of the water column. Similarly, shallow and deep cross-frontal eddy heat fluxes also nearly balance: this cancelation appears to help explain how the classical one-dimensional potential energy criterion for frontal location can work so well in a complex ocean.

1. Introduction

Georges Bank, a tidally well-mixed region off the northeastern United States, is noted for its sustained high biological primary productivity (e.g., O'Reilly et al., 1987). Maintaining productivity on seasonal time scales appears to require some sustained nutrient flux from deeper ambient waters into the well-mixed region. Franks and Chen (1996: referred to as FC hereafter) have presented a two-dimensional (cross-isobath and vertical) physical-biological numerical model that accounts for such a flux. Their model is driven by imposed tidal fluctuations that create both a tidally mixed area and energetic variability in the front that separates mixed from ambient waters. A mixture of mean flow, eddy fluxes and other

1. Department of Physical Oceanography, Mail Stop 21, Woods Hole Oceanographic Institution, Woods Hole, Massachusetts 02543 USA.
2. Corresponding author ***e-mail: kbrink@whoi.edu***

mechanisms (that Hu et al., 2008 call collectively "tidal pumping") appears to account quantitatively for the required nutrient fluxes in their model.

Although the two-dimensional FC model is successful by any measure, there remains a question. Many fronts found in the ocean are unstable to along-front variations, and there is certainly evidence that tidal mixing fronts are at least sometimes unstable (e.g., Simpson and James, 1986; Badin et al., 2009). Interestingly, though, three-dimensional extensions of the FC model for Georges Bank (Franks and Chen, 2001; Hu et al., 2008) do not show any obvious sign of frontal instability. Idealized models of tidal mixing fronts (e.g., van Heijst, 1986; Thomas and Linden, 1996; James, 1989; Pasquet et al., 2012) certainly show a baroclinic-type instability, but these models do not always include complexities of the real ocean such as tidal fluctuations or energetic vertical mixing. Simulation models for the waters around the British Isles, however, do result in unstable tidal mixing fronts under realistic circumstances (Badin et al., 2009). Thus, one might ask about the existence of instabilities of tidal mixing fronts around Georges Bank.

If these instabilities occur, they ought to give rise to a cross-frontal eddy flux of nutrients (among other properties). Thus, the general question arises as to how strong the consequent lateral eddy fluxes might be in a tidal mixing front, and whether these fluxes can play a substantial role in biological processes compared to the two-dimensional processes encapsulated in FC. In this sprit, a sequence of idealized studies was undertaken, starting with the linear and nonlinear stability of a very idealized tidal mixing front that lacks both tidal currents and strong boundary layer mixing (Brink, 2012). The parameter and structural sensitivities explored with this model show that all frontal configurations considered are unstable to some degree and that the finite amplitude eddies follow an inverse cascade towards larger, more barotropic eddies. The present contribution takes a considerable step toward reality by treating the case with tidal currents and strong boundary layer turbulence. This allows treatment of a less idealized frontal instability, the resulting mixing, and their parameter dependence.

2. Approach

All numerical calculations are carried out using the hydrostatic, primitive equation Regional Ocean Modeling System (ROMS: e.g., Haidvogel et al., 2000; Shchepetkin and McWilliams, 2005). The governing equations for the model as configured are:

$$u_t + uu_x + vu_y + wu_z - fv = -\rho_0^{-1} p_x + (A_{u_z})_z \tag{1a}$$

$$v_t + uv_x + vv_y + wv_z + fu = -\rho_0^{-1} p_y + (Av_z)_z \tag{1b}$$

$$0 = -p_z - g\rho \tag{1c}$$

$$u_x + v_y + w_z = 0 \tag{1d}$$

$$\rho_t + u\rho_x + v\rho_y + w\rho_z = (B\rho_z)_z \tag{1e}$$

$$\rho = \rho_0[1 - \beta(T - T_0)] \tag{1f}$$

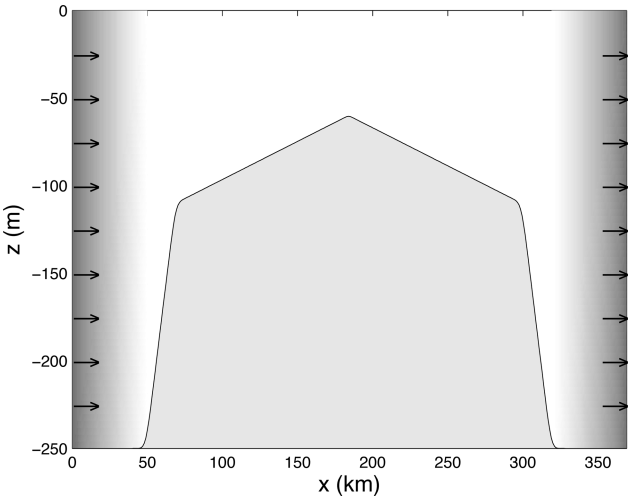

Figure 1. Cross-section of the numerical domain. The shaded areas on the edge denote the location of the sponge layers.

where (x, y, z) are the cross-channel, along-channel and vertical coordinates, respectively, and (u, v, w) are the corresponding velocity components. Pressure is p, temperature is T, density is ρ, the Coriolis parameter is f, and a constant reference density is ρ_0. Time is t, and subscripted independent variables represent partial differentiation. The acceleration due to gravity is g, T_0 is a reference temperature (14 °C), the thermal expansion coefficient for water is $\beta(= 1.7 \times 10^{-4}\ ^\circ\mathrm{C}^{-1})$, and the vertical turbulent viscosity and mixing coefficients A and B, respectively, are found using the Mellor-Yamada level 2.5 turbulence closure scheme (e.g., Wijesekera et al., 2003). Sensitivity tests using the k-ε turbulence closure scheme did not yield substantially different results. There is no explicit lateral mixing or viscosity in any model run aside from a lateral sponge layer near the open boundaries. The system is solved with a free surface boundary condition, and no flow passes through the bottom. No turbulent heat fluxes are allowed through any boundary. The bottom boundary condition uses a quadratic stress:

$$A(u_z, v_z) = c_D(u^2 + v^2)^{1/2}(u, v), \tag{2}$$

where c_D is a drag coefficient. At the surface, most runs do not have any applied stress.

The model geometry (Fig. 1) has a symmetric, high bank, and the model mimics tidal forcing by having a depth-averaged flow through the open boundaries at $x = 0$ and L:

$$\bar{u} = u_0 R(t) \sin(\omega t) \tag{3a}$$

where $R(t)$ allows a ramping-up of the tidal forcing:

$$R = 0.5[1 - \cos(\pi t/t_R)] \qquad \text{for } 0 < t < t_R \tag{3b}$$

$$R = 1 \qquad \text{for } t > t_R. \tag{3c}$$

The ramp time t_R is held at two days. The channel is cyclic in the along-isobath direction. A 50 km wide sponge layer, where the lateral mixing coefficient and viscosity increase from 0 to 250 $m^2\ sec^{-1}$, occurs near (over a 50 km range) each open boundary. At the boundary, either a radiation condition (for free surface height) or no-normal gradient condition (for temperature or depth-dependent velocity) is also applied. This model configuration, with relatively deep water near the forcing boundaries, minimizes the effects of nonlinear, tidally generated internal waves originating at the bank edges. For all model runs, results will only be considered for the uniformly sloping region for $x > L/2$ (i.e., for $184 < x < 299$ km). Tests show that this "shelf" region is sufficiently wide that results for stability or consequent fluxes do not depend on the sloping region's width. The along-channel grid resolution is 0.25 km, and the cross-channel resolution varies slowly from 0.66 km at the channel center to 1.06 km at the outer boundary. In the vertical, 30 grid points are located on a stretched grid that allows best resolution near the surface and especially in the bottom boundary layer. The channel is 50 km long for all three-dimensional runs reported here.

A total of 21 model runs (Table 1) were carried out for at least 52 model days, each done both two-dimensionally and three dimensionally. All runs were long enough to allow at least 20 days of relatively statistically stable results at the end. Three additional runs were executed only in the two-dimensional mode. For each run, eddy kinetic energy (where "eddy" is defined relative to an along-channel mean) is computed over the range of $x =$ 210–265 km, which always includes the frontal position once finite-amplitude instability is reached. This definition means that eddy kinetic energy is always zero in two-dimensional runs. Frontal location is defined as the location of maximum cross-channel temperature gradient at the surface. For all model runs, a lateral eddy mixing coefficient is calculated as

$$K = -<u'T'>/<T_x> \tag{4}$$

using vertical averages over the lower part of the water column, defined by the temperature gradient being negative and the flux being down-gradient. In this case, (u', T') are deviations from the mean over along-channel distance and a tidal period, denoted by $< >$. This definition means that the mixing coefficient can be non-zero even in two-dimensional runs. Estimates are made at the mean location of the front over nominally the last 20 days, x_f, and at locations 2 and 5 km on either side. (The averaging interval is "nominal" because the averaging is actually over the largest integral number of tidal cycles that fit into the last 20 days). The mean of these five values is saved for further analysis. Other diagnostics include an estimate of the along-channel wavelength (estimated as four times the distance

Table 1. Summary of model runs

Run Number	f ($\sec^{-1}$) $\times 10^4$	α $\times 10^3$	T_z ($^\circ$ m^{-1})	C_D $\times 10^3$	u_0 (m sec^{-1})	Period (hours)	h_f (m)	EKE (m^2 sec^{-2}) $\times 10^3$	K_{H2} (m^2 sec^{-1})	K_{H3}
1	2	1.0	0.14	10	0.26	12.42	95	2.46	56	139
2	1	1.0	0.14	10	0.26	12.42	106	3.26	138	257
3§	1	1.0	0.14	5	0.26	12.42	113	4.11	112	270
4	1	1.0	0.04	10	0.26	12.42	118	1.46	112	174
5	1	1.0	0.14	10	0.20	12.42	115	0.78	68	91
6	1	1.0	0.14	10	0.26	24.84	109	3.82	83	324
7	1	1.0	0.14	10	0.18	49.68	114	1.42	94	143
8*	1	1.0	0.14	10	0.16	12.42	87	1.83	103	145
9	1	1.0	0.14	10	0.22	18.63	105	7.19	26	155
10*	1	1.0	0.07	10	0.12	12.42	84	0.92	62	93
11*§	1	1.0	0.14	5	0.15	12.42	77	1.80	128	169
12*	1	1.0	0.14	10	0.14	18.63	83	3.50	19	103
13	0.5	1.0	0.14	15	0.32	12.42	115	0.10	201	424
14*	0.5	1.0	0.16	10	0.18	12.42	87	0.09	105	202
15	1	0.43	0.19	10	0.15	12.42	83	1.99	115	158
16	2	0.43	0.14	10	0.178	12.42	86	0.68	22	43
17	1	0.43	0.19	5	0.16	12.42	80	2.39	109	149
18	1	0.43	0.19	2	0.205	12.42	80	3.04	188	200
19	1	1.0	0.14	5	0.26	24.84	107	3.46	205	285
20	2	1.0	0.08	5	0.32	12.42	109	1.07	37	62
21*	1	0.43	0.07	5	0.07	12.42	59	0.37	61	59
101*†	1	1.0	0.08	5	0.08	12.42	63	–	47	–
102*†	1	1.0	0.14	10	0.05	12.42	50	–	39	–
103*†	1	1.0	0.18	5	0.04	12.42	41	–	32	–

*Depth = 36 m at the top of the bank. For all other runs, the shallowest depth is 60 m.
†Only a two-dimensional run was done in this case, to establish h_f for a range of smaller depths.
§Runs duplicated using models including biology.

to the first zero-crossing of the along-channel covariance function for u), an along-channel propagation speed (estimated from lagged y correlations of u records offset in time), and energy conversions from mean to eddy energy.

3. Model Results

Run 17 (Table 1) provides fairly representative results. As in all cases, the model ocean starts out stably stratified and at rest. Once tidal currents start, they reach O(1 m sec^{-1}) near the center of the bank, and the resulting near-bottom turbulence leads to the development of a surface-to-bottom front. As time advances, the bottom mixed layer continues to deepen slowly, and the front migrates into deeper water (Fig. 2). The front regularly moves over

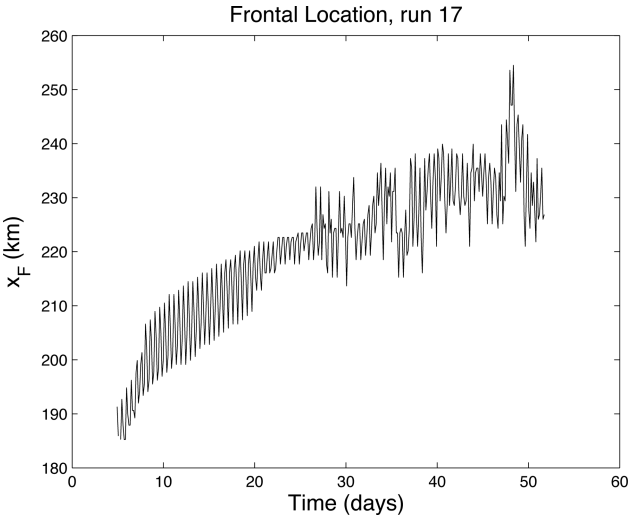

Figure 2. Position of the surface tidal mixing front for run 17 at $y = 0$ km. The instability reaches finite amplitude around day 20–25 (see Fig. 5).

a cross-isobath range of order 10 km during each tidal cycle, and the values h_f (the water depth at the frontal location, as estimated from the numerical model) in Table 1 represent averages over nominally the last 20 model days of a run. As might be expected from a well-mixed layer, the bottom boundary layer develops a well-defined cap which intersects the free surface as the front (Fig. 3). Averaged over a tidal cycle, the mean along-channel flow is strongest near the top of the bottom boundary layer. This structure is explained by a thermal wind balance with the horizontal density gradient associated with boundary layer mixing above a sloping bottom (e.g., Brink and Lentz, 2010: BL henceforth). The contribution to this mean flow by barotropic tidal rectification (e.g., Loder, 1980) is an order of magnitude weaker in the stratified region.

By the last 20 days, the two-dimensional model runs stop evolving, other than sometimes a continued slow drift of the front into deeper water. In contrast, all three-dimensional model runs become unstable as manifested, for example, by surface frontal position (e.g., Fig. 4). The instabilities generally reach finite amplitude after day 20 and before day 50. In most cases, the "baroclinic" conversion of potential to kinetic energy,

$$C_{PE\rightarrow KE} = \frac{1}{V}\iiint \frac{g}{\rho_0} < w\rho > dV \tag{5}$$

(where V is the volume) is the dominant source of eddy energy, (e.g., Fig. 5), sometimes by orders of magnitude. The "barotropic" conversions associated with mean to eddy kinetic energy transfer,

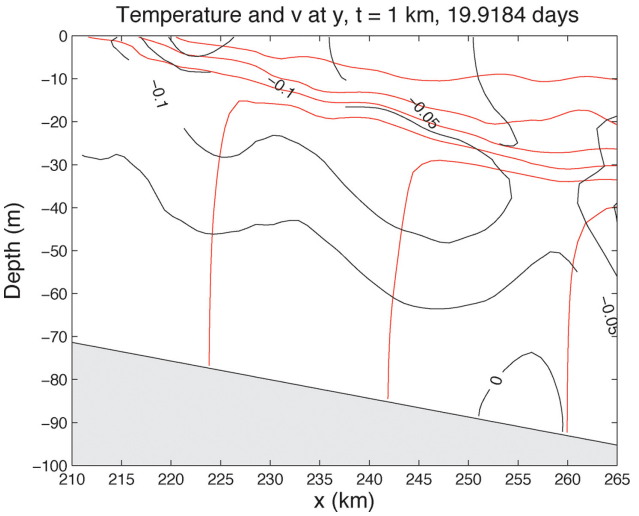

Figure 3. Along-channel velocity (solid contours) and temperature (red contours) for run 17 at $y = 1$ km, at $t = 20$ days. Velocity and temperature are averaged over a single tidal period to remove the dominating tidal current. The contour interval for temperature is 2°.

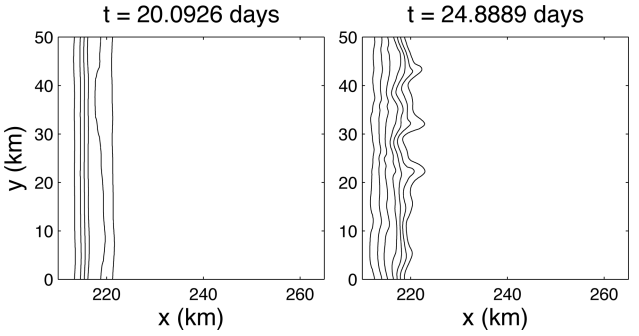

Figure 4. Initial evolution of surface temperature for run 17: days 20 (left) and 25 (right).

$$C^{H}_{MKE\rightarrow EKE} = -\frac{1}{V}\iiint \left[< u'v' >< v_x > + < u'u' >< u_x >\right] dV, \tag{6a}$$

$$C^{V}_{MKE\rightarrow EKE} = -\frac{1}{V}\iiint \left[< v'w' >< v_z > + < w'u' >< u_z >\right] dV \tag{6b}$$

are stronger in a few cases (runs 5, 7, 9 and 10). All model runs show a substantial baroclinic energy conversion before the instability reaches finite amplitude, e.g., before day 20 in Figure 5. This conversion is apparently associated with the development of the thermal-wind balanced mean flow once vertical mixing in the bottom boundary layer creates horizontal density gradients.

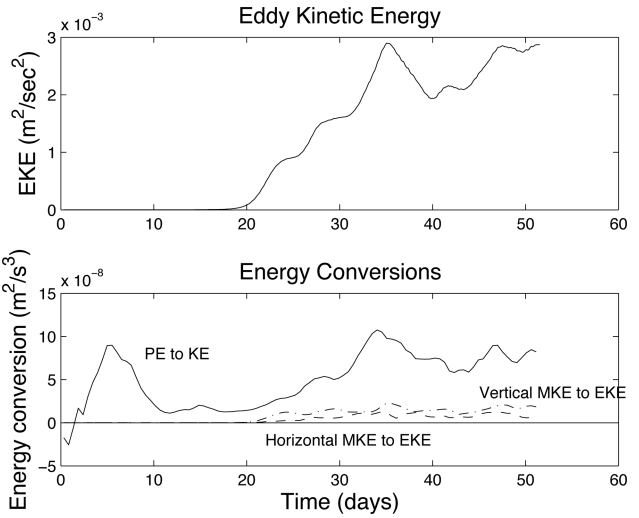

Figure 5. Upper panel: eddy kinetic energy per unit mass for run 17, volume averaged over $x = 210$–265 km. Lower panel: Energy conversions averaged over the same volume. Solid line: potential energy to total kinetic energy, Dashed line: mean kinetic energy to eddy kinetic energy conversion due to horizontal eddies, Dash-dot line: mean kinetic energy to eddy kinetic energy conversion due to vertical eddies.

Typically, the initial instability has an along-channel wavelength of 8–24 km, although a couple runs (13 and 14) with low Coriolis parameter, hence large Rossby Radius, have wavelengths comparable to the channel length. The initial wavelength in fact scales well (correlation 0.85) with an estimated internal Rossby radius of deformation, $Nh_f f^{-1}$, where N is the initial buoyancy frequency. With time, the wavelength typically increases somewhat (Fig. 6), but never as dramatically as in the frictionless initial value problem (Brink, 2012). The baroclinity of the flow is estimated using the ratio

$$\Gamma(t) = \frac{SD[u(x, y, 0, t) - u(x, y, -h/2, t)]}{SD[0.5\{u(x, y, 0, t) + u(x, y, -h/2, t)\}]}, \tag{7}$$

(where SD represents the standard deviation in the y direction), area averaged over $x = 210$–265 km and all y. This remains near two throughout all model runs. For perspective, an $n = 1$ baroclinic mode has $\Gamma = 2$ and barotropic flow has $\Gamma = 0$. Thus, there is no evidence of the flow becoming barotropic (as in the unforced initial value problem: Brink, 2012) with time. The vertical structure of the eddy field is characterized with empirical orthogonal functions. Although strongly vertically sheared everywhere, the eddies are surface intensified on the mixed side of the mean frontal location, but intensified at mid-depth on the stratified side. Near the mean frontal location, there is generally a zero-crossing in the lower part of the water column (i.e., generally within the bottom boundary layer). Thus, the Pasquet et al. (2012) characterization of frontal eddies as hetons would be an

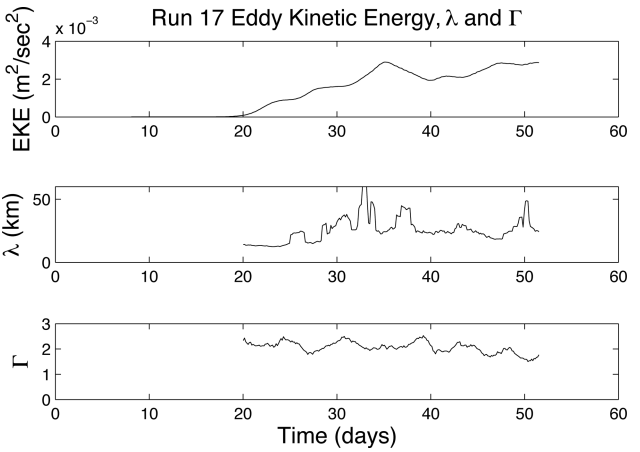

Figure 6. Evolution of eddy kinetic energy per unit mass (volume averaged from $x = 210$ to 265 km), along-channel wavelength λ and surface intensification ratio Γ for run 17.

oversimplification in the present context. The absence of strong vertical or horizontal scale evolution is perhaps not surprising for these model runs, which are continually being forced and damped: there is no opportunity to enter a freely evolving inverse scale cascade toward an equilibrium state.

All runs are carried out long enough that there is at least a 20-day period of sustained finite-amplitude eddy kinetic energy, e.g., after day 30 in Figure 6. It is over this period that statistical properties such as mean eddy kinetic energy (Table 1) or eddy mixing coefficient (Equation 4, Table 1) are estimated. Once the instability has reached this finite-amplitude state, it does not proceed so far as to destroy the front, but the eddies do distort it and cause considerable time dependence (e.g., Fig. 7). In particular, the sharpness of the front varies greatly from place to place. In all cases, the frontal meanders and eddies propagate toward negative y at a rate of 2–9 km day^{-1} (depending on the particular model run).

It is worth asking why the present three-dimensional model runs always result in an unstable tidal mixing front, but more realistic models, such as that of Hu et al. (2008) do not result in any evident instability. The stated grid resolution in Hu et al. is 0.5–1 km near the tidal mixing front, as compared to the 0.25 (along-isobath) or 0.66–1.06 km (cross-isobath) used here. The present model runs yield most unstable wavelengths of typically 8–24 km, so the Hu et al. grid resolution is probably capable of resolving the instability at some level. Further, Hu et al. (2008) used lateral eddy coefficients of 30–500 m^{2}sec^{-1}, depending on location. Repeating run 17 with these two end-member eddy coefficient values makes no difference in instabilities (measured, for example by eddy kinetic energy). Hu et al. (2008) apparently used model runs roughly 50 days in length, which ought to allow enough time for instabilities to reach finite amplitude. The Chen et al. (2008) results do implicate resolution and diffusivity, in that their simulation runs do not replicate observed dye patch evolution

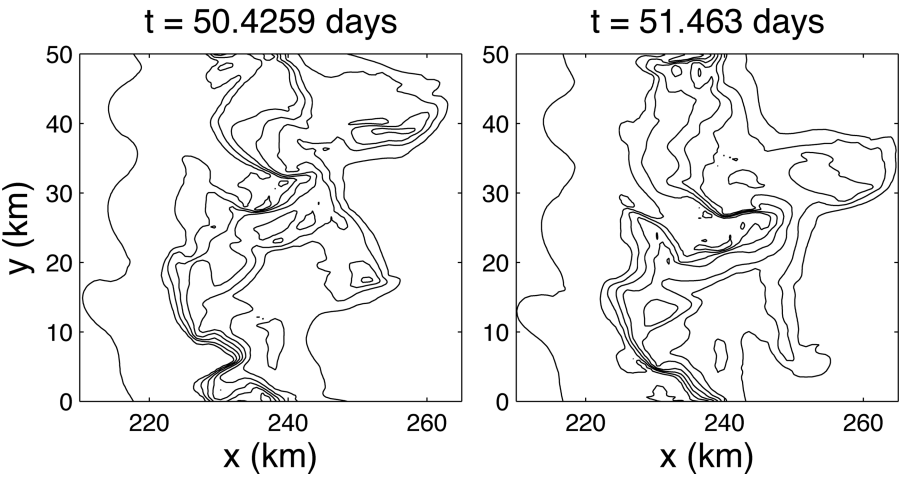

Figure 7. Surface temperature for run 17 at days 50.4 (left) and two tidal periods later, at day 51.6 (right). Contour interval = 1°.

well until grid resolution and lateral diffusivity are reduced to about 0.5 km and 20 m^2 sec^{-1}, respectively. Another effect might lie in the fact that the front on the northern slope of Georges Bank lies at the shelfbreak, rather than in the middle of a uniformly sloping region. Preliminary numerical experiments where the front is at the shelf/slope junction suggest enhanced, not weakened, instabilities relative to the case with planar geometry. Thus, the frontal location does not rationalize the difference. Altogether, it is not obvious why the Hu et al. (2008) or similar runs do not display instabilities, although resolution seems plausible and the more irregular bottom topography on a more realistic Georges Bank might be a factor.

In the real ocean, the interplay of different tidal species leads to spring-neap cycles in tidal amplitude, hence frontal location (e.g., Loder et al., 1993). This issue was explored briefly. In the two-dimensional case, the front tends to move offshore when tides reinforce positively, and then remain in place during the weaker phase of the tides. The fact that the front does not move back and forth with the spring-neap cycle is not surprising, in light of the absence of a surface heat flux, which acts to restratify the ocean water and so let the front migrate into shallower water when tides are weaker. Nonetheless, the variable tidal amplitudes are associated with changes in lateral diffusivity and eddy kinetic energy. The spring-neap modulation is not pursued any further, however, because meaningful results would require the addition of a surface heat flux, hence a broader parameter space.

One might ask how the cross-channel property fluxes occur. In the two-dimensional case, which is equivalent to the FC problem, the obvious candidates are transport by the mean cross-channel flow, and "eddy" fluxes associated with unsteady (but uniform along isobaths) motions. The steady flow would be associated with bottom Ekman transport and an

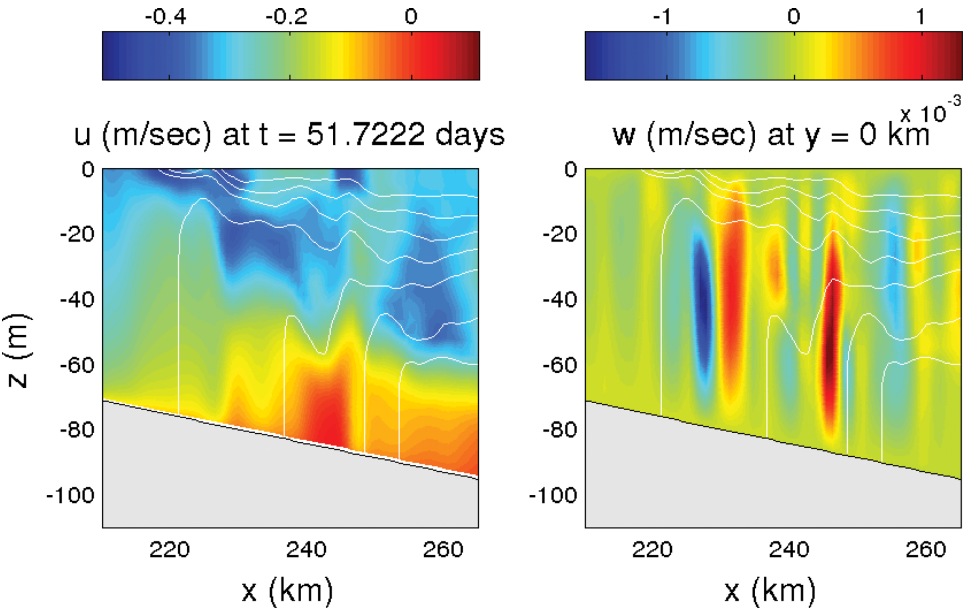

Figure 8. Sections of instantaneous cross-channel (left) and vertical (right) velocity for the two-dimensional version of run 17 at day 51.7. The white contours represent temperature at increments of 2°C. Because tidal currents are included in the u field, the circulation cells are most obvious in the alternating patterns in w.

ageostrophic interior return flow (e.g., Garrett and Loder, 1981; Loder and Wright, 1985). In general, both steady and unsteady contributions play a substantial role in generating fluxes, and neither ever dominates. Although one might expect that the two-dimensional "eddy" transport might be associated with time-dependent shear dispersion (e.g., Young et al., 1982), scaling analysis (see the next section) shows that the transport appears instead to be associated more with overturning cells that are primarily confined to the bottom boundary layer (Fig. 8). These cells, and their related eddy heat transport, obey a scaling consistent with their being caused by symmetric instabilities (e.g., Stone, 1966). In the three-dimensional case, eddy transport is enhanced by the pseudo-baroclinic instabilities. This enhancement is made obvious by comparing the lateral eddy transport coefficients from two-dimension models runs, K_{H2}, with those from identical, but three-dimensional runs, K_{H3}. Table 1 shows that K_{H3} is often at least double the two-dimensional equivalent.

4. Parameter Dependence

a. Frontal location

In the absence of surface buoyancy fluxes, the tidal mixing front ought to appear at the location where the water depth is equal to the thickness of the bottom boundary layer. An

estimate H_f of this thickness for a case with fluctuating currents over a sloping bottom is (BL)

$$H_f = \mu u_T^* G N^{-1/2} \tag{8}$$

where μ is a constant (found to be 1.3 in BL), u_T^* is the friction velocity associated with the tidal currents, G is a function of frequency (ω) and Coriolis parameter that is related to boundary layer structure, and N is the buoyancy frequency above the bottom boundary layer (i.e., the initial buoyancy frequency). H_f is an approximation to the computed value h_f. The bottom slope α appears in the expression through

$$f^* = f(1 + s^2)^{1/2}, \tag{9a}$$

$$\omega^* = \omega(1 - s^2/\sigma^2), \tag{9b}$$

$$s = \alpha N/f \tag{9c}$$

$$\sigma = \omega/f, \tag{9d}$$

$$G = (f^2 + \omega^{*2})^{1/4} |f^{*2} - \omega^2|^{1/2}. \tag{9e}$$

Expression (9e) neglects the BL boundary layer damping term, which does not improve the expression's skill in the present case. The amplitude of the tidal friction velocity is given, using BL, as

$$u_T^* = b c_D{}^{1/2} F(\omega) u_T \tag{10a}$$

where u_T is the local tidal current amplitude. Assuming that the tidal transport is conserved (*i.e.*, $u_T = u_0 h_0 H_f^{-1}$: e.g., Loder, 1980) then leads to

$$u_T^* = b c_D{}^{1/2} F(\omega) u_0 h_0 / H_f \tag{10b}$$

where u_0 is the tidal amplitude at the open boundary, and h_0 is the water depth at the boundary. The function $F(\omega)$ accounts for changes in the bottom boundary layer structure near the inertial frequency

$$F(\omega) = 1 - e^{-\theta |f^* - \omega|/f^*}. \tag{10c}$$

This form for F differs from that of BL because their interior flow is strictly rectilinear (along isobaths), but the tidal currents in the present case follow ellipses.

The expressions (8–10) are used to estimate the water depth at the tidal mixing front, and are compared to the computed h_f values (Table 1) from model runs. For the 24 two-dimensional model runs (Fig. 9), $\mu = 1.45$ (correlation = 0.94 with $\theta = 8$, compared to BL's $\theta = 7.5$), and for the 21 three-dimensional runs, $\mu = 1.56$ (correlation 0.91 with $\theta = 4$). It is probably not surprising that the parameters agree no better with the BL pseudo one-dimensional calculations because of differences in vertical grid resolution and the present model's inclusion of a wider range of potential lateral transport processes.

b. Eddy kinetic energy

Eddy kinetic energy, because it is defined relative an along-channel mean, is only present in the three-dimensional model runs. In the case of an unforced, initial value problem (Brink, 2012), it is reasonable to use the initial available potential energy as a basis for scaling. In the present problem, however, turbulent mixing creates lateral density gradients within the bottom boundary layer (e.g., Fig. 3), so that available potential energy can continually be created. Further, the eddy kinetic energy generated by the frontal instability is continually being dissipated because the strong tidal currents assure a substantial bottom stress (e.g., Wright and Thompson, 1983). Thus, it appears that an appropriate starting point for scaling eddy kinetic energy is to compare the creation of available potential energy to the dissipation of the eddy kinetic energy generated by the instability.

As a further simplification, it is convenient to conjecture that the creation of available potential energy is proportional to the creation of total potential energy. Then, it is also assumed that this rate can be treated locally (or averaged over a large domain). Under these assumptions, the balance of potential energy creation and eddy dissipation can be stated as

$$\gamma \int_{-h}^{0} BN^2 \rho_0 dz = \vec{v}_D \cdot \vec{\tau}_D \tag{11}$$

where B is a turbulent vertical eddy diffusivity, γ is an unknown constant, and subscript D represents a quantity evaluated at the bottom. For the sake of being definite, the water depth h will be taken as that at the frontal location. The turbulent vertical diffusivity can be (over)approximated using a law of the wall scaling by

$$B = O(u_T^* h_f) \tag{12}$$

where the friction velocity associated with the tidal currents is given by (10a).

Following the logic of Wright and Thompson (1983), the bottom stress magnitude associated with the eddy flow u_E is roughly

$$\tau_D = \mathrm{O}(\rho_0 C_D u_T u_E b^2 F^2). \tag{13}$$

Approximating the integral in (11) as multiplication by h_f, an approximation to a typical eddy current magnitude can be found as:

$$u_E^2 = \gamma' \frac{h_f^2 N^2}{F(\omega)\sqrt{c_D}}. \tag{14}$$

However, it is found that, as in the inviscid initial value problem (Brink, 2012), the instability is inhibited by the positive bottom slope, and this can be accounted for inserting an empirical term that depends on s (although the correction used here is not the same as that of Brink,

2012 where bottom slopes of either sign are treated). Thus, an appropriate scaling for eddy kinetic energy per unit mass is

$$EKE = \gamma'' \frac{h_f^2 N^2}{F(\omega)(1 + cs^2)\sqrt{c_D}}. \tag{15}$$

An alternative expression is obtained by substituting (8) for h_f in (15), so that the result is expressed in terms of the far-field tidal amplitude:

$$EKE = \gamma''' \frac{h_0 u_0 N^{3/2}}{1 + c's^2} G. \tag{16}$$

Both of these expressions are evaluated against the 21 three-dimensional model runs of Table 1. For the first expression (15), the values $c = 3, \gamma'' = 8.7 \times 10^{-5}$ yield a correlation of 0.85 and rms error 0.0011 m^2 sec^{-2}. The second expression (16) with $c' = 7, \gamma''' = 2.6 \times 10^{-4}$ gives a better approximation with a correlation of 0.92 and rms error 0.0009 m^2 sec^{-2}.

It is worth noting that the bottom slope correction (s^2 term) only makes a modest, 2–10%, improvement to the fit. One other peculiarity about this scaling is that one might expect the coefficients γ'' or γ''' to be O(1). The explanation is apparently the over-approximation in (12) and perhaps the accumulation of a number of empirical coefficients such as b^2 or γ that are generally somewhat less than 1.

c. Lateral mixing coefficient

Two dimensional case: In the two-dimensional case, the down-gradient transport across the front appears to be associated with nearly vertical, but slantwise, convection rolls in the bottom boundary layer (e.g., Fig. 8). The relevant length scale can be estimated by considering the very simple case of the linear instability of a uniformly stratified, unbounded ocean with geostrophically balanced flow (that has uniform vertical shear). In this case, the most unstable wave (e.g., Stone, 1966) occurs when

$$\frac{k}{m} = \frac{f U_z}{N_0^2} \tag{17a}$$

where U is the mean velocity (U_z is a constant), and (k, m) are the cross-stream and vertical wavenumbers of the instability. Here, the buoyancy frequency N_0 is the buoyancy frequency within the bottom boundary layer. The growth rate φ is then given by

$$\varphi^2 = f^2 \left(\frac{1}{Ri} - 1 \right) \tag{17b}$$

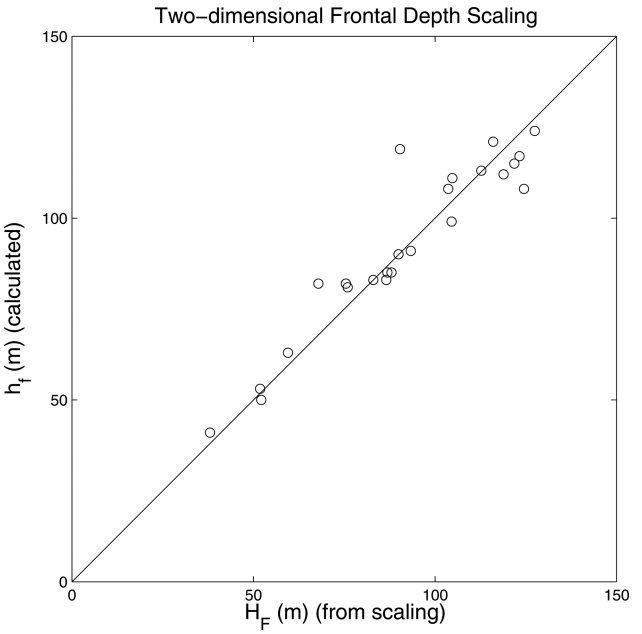

Figure 9. Scatter plot comparing the scaling H_f (8–10) for water depth at the front to results of two-dimensional numerical model runs. The correlation of the fit is 0.94 and the rms error is 8.4 m.

where Ri is the gradient Richardson number N_0^2/U_z^2. Estimating the vertical wavenumber in (17a) as $2\pi/\delta$ (where δ is the bottom boundary layer thickness), and using $Ri < 1$ for instability, yields a bound for the horizontal length scale

$$L \leq O\left[\frac{\delta U_z}{f}\right]. \tag{18}$$

The water depth at the front h_f will now be taken as representative of the boundary layer thickness δ.

The lateral mixing coefficient is conjectured to scale as a representative tidal velocity times the slantwise convection length scale L. Thus, near the tidal mixing front,

$$K_{H2} \approx a\frac{u_0 h_0 L}{h_f} \tag{19}$$

and, estimating U_z as $u_0 h_0/h_f^2$,

$$K_{H2} \leq O\left[\left(\frac{u_0 h_0}{h_f}\right)^2 \frac{1}{f}\right]. \tag{20}$$

Finally, the expression (8) can be used to approximate the frontal depth, and the inequality in (20) taken to be a reasonable estimate at magnitude, so that

$$K_{H2} \approx \gamma_2 \frac{u_0 h_0}{f^* FG} \sqrt{\frac{N}{c_D}} \tag{21}$$

where γ_2 is an unknown constant. This expression is tested against the 24 two-dimensional model runs (Table 1), and, with $\gamma_2 = 0.013$, the correlation of the fit is 0.75 with an rms error of 32 m^2 sec^{-1}. This scaling is the best of several that were tried, and is far better than any scaling based on time-dependent shear dispersion (e.g., Young et al., 1982).

Three dimensional case: In three-dimensional model runs, a frontal instability always occurs, so the scaling for a lateral mixing coefficient is based on the idea that the eddy heat flux is dominated by the resulting eddies. In this case, the eddy coefficient is taken to be an eddy kinetic energy scale (16) times a representative time scale f^{*-1}. Thus,

$$K_{H3} = \gamma_3 \frac{u_0 h_0 FGN^{3/2}}{f^*} \frac{1}{1 + c'' s^2}. \tag{22}$$

This expression is evaluated against the 21 three-dimensional model runs of Table 1. The best fit (correlation 0.92, rms error = 36 m^2 sec^{-1}) is obtained with $\gamma_3 = 0.0020$ and $c'' = 4$.

Comparing expressions (21) and (22) for the lateral mixing coefficient shows that frontal instability becomes increasingly dominant relative to two-dimensional effects as $Nc_D^{-1/2}$ increases, hence, from (16), as eddy kinetic energy increases. This, of course, is consistent with the idea that for a given frontal configuration, the pool of available potential energy increases as the ambient stratification increases.

5. Sample Biological Calculations

a. Formulation

The physical analysis of the preceding sections shows that frontal baroclinic instability increases lateral exchange near the tidal mixing front. It is thus appropriate to carry out a few model runs that include a simple biological model, similar to that of FC, in order to evaluate the biological impact. It should be noted at the outset that even a simple NPZD (Nutrient-Phytoplankton-Zooplankton-Detritus) model introduces about 12 new parameters, and thus a very wide parameter space that could be explored. A conscious choice is made here only to use essentially the FC parameter choices. Undoubtedly, there may be other credible choices for these parameters for this region, but exploring this range would call for real biological expertise. In this regard, it is encouraging that Franks and Chen (2001) report that their results are relatively insensitive to at least some of the biological model's parameters.

Table 2. Parameters in the biological model system

Parameter	Description	Value
V_m	Maximum nutrient uptake rate	2 d^{-1}
k_N	Inverse Half-saturation constant for nutrient uptake	1 mmole nitrogen m^{-3}
R_m	Maximum zooplankton grazing rate	0.5 d^{-1}
ς_{mr}	Zooplankton death rate converting to nutrient pool	0.2 d^{-1}
ς_{md}	Zooplankton death rate converting to detritus	0.0 d^{-1}
k_p	Phytoplankton saturation coefficient (in grazing term)	3 mmole nitrogen m^{-3}
r_d	Rate for detritus breakdown to nutrients	2 d^{-1}
p_m	Phytoplankton death rate	0.1 d^{-1}
g_a	Zooplankton grazing inefficiency	0.7
e_c	Zooplankton excreted fraction	0
k_{ext}	Diffuse light attenuation coefficient	0.1 m^{-1}
w_s	Phytoplankton sinking rate	-1.0 m d^{-1}

Adding the biological model to the system, using the current ROMS "NPZD_FRANKS" option introduces four new governing equations:

$$Nut_t = Phys(Nut) - \frac{NutPV_m \exp(k_{ext}z)}{k_N + Nut} + e_c \frac{ZP^2R_m}{k_P^2 + P^2} + \zeta_{mr}Z + r_d D \tag{23a}$$

$$P_t = Phys(P) + \frac{NutPV_m \exp(k_{ext}z)}{k_N + Nut} - p_m P - \frac{ZP^2R_m}{k_P^2 + P^2} - w_S P_z \tag{23b}$$

$$Z_t = Phys(Z) + (1 - g_a)\frac{ZP^2R_m}{k_P^2 + P^2} - \zeta_{mr}Z - \zeta_{md}Z \tag{23c}$$

$$D_t = Phys(D) + \frac{ZP^2R_m}{K_P^2 + P^2}(g_a - e_c) - r_d D + p_m P + \zeta_{md}Z \tag{23d}$$

where Nut, P, Z, and D represent the concentrations of nutrient, phytoplankton, zooplankton and detritus (all expressed as mmoles nitrogen m^{-3}), and "$Phys(q)$" represents physical transport:

$$Phys(q) = -uq_x - vq_y - wq_z + (Bq_z)_z. \tag{23e}$$

The non-physical processes in (23a) respectively represent nutrient consumption due to phytoplankton growth, nutrient resupply associated with zooplankton grazing, dying zooplankton converted directly to nutrient, and the conversion of detritus into nutrients. The phytoplankton equation (23b) also includes terms associated with mortality ($p_m P$) and sinking ($w_S P_z$). The zooplankton equation (23c) includes a term representing dying zooplankton that are converted to detritus ($\varsigma_{md} Z$). The various constants are given in Table 2.

The present governing biological equations differ from those of FC in two ways. First, they use a different expression to govern the zooplankton grazing rate:

$$1 - \exp(-\lambda P) \tag{24a}$$

as opposed to the present form:

$$\frac{P^2}{k_P^2 + P^2}. \tag{24b}$$

The coefficient $k_p = 3$ mmole nitrogen m^{-3} was thus chosen to make the present form nearly match (24a) with the FC value $\lambda = 0.2(\mu\text{mole nitrogen } l^{-1})^{-1}$. Secondly, the FC calculations do not include a detritus pool. For the present calculations, the detritus pool is retained, but it is given a very short time scale ($r_d = 2d^{-1}$) for the conversion from detritus to nutrients. Further, no mortality transfer from zooplankton to detritus is allowed: dead zooplankton are converted directly to nutrients. The short detritus residence time scale should lead to results similar to those of FC where, for example, dying phytoplankton are transferred directly to the nutrient pool.

All model runs are initialized in a form similar to that of FC. P is constant at 4 m mole nitrogen m^{-3} in the upper 20 m, and 0 below 25 m. Z increases from 0 below 25 m up to 2.5 m mole nitrogen m^{-3} at the surface, $D = 0.5$ m mole nitrogen m^{-3} at all depths, and *Nut* = (7.0 m mole nitrogen $m^{-3} - P - Z$). Values of *Nut, P, Z* and D at the lateral boundaries are clamped to the initial values, and there are no diffusive fluxes through the surface or bottom. Thus, in contrast to Badin et al. (2010) for example, there is no benthic recycling. All model runs are carried out for 51.5 days. In contrast, the FC model runs were only carried out for about 25 tidal periods (about 12.9 days). While the present model runs agree qualitatively with the FC runs at 12.9 days, some changes occur during the longer runs. Specifically, by day 51, the zooplankton levels decrease to less than about 0.1 m mole nitrogen m^{-3}, so zooplankton largely cease to play a substantial role in the problem. Also, while there is a pronounced subsurface chlorophyll maximum in stratified waters at day 12.9, this maximum is less consistently present at later times: the highest phytoplankton populations are generally found in the well-mixed waters.

b. Results

About 20 two-dimensional model runs were carried out to explore the sensitivity of model results to the turbulence closure scheme, a few biological rates, or along-bank wind stress. Several variants of the Mellor-Yamada level 2.5 turbulence closure scheme were tested, along with the k–ε (Wijesekera et al., 2003) scheme. All of these mixing schemes yielded qualitatively similar results, with time- (nominally the last 20 days of the run) and volume-integrated ($x = 210$ to 265 km: a range that consistently samples both sides of the front) phytoplankton stock varying by about 1–15%, depending on the particular scheme. If particles are not allowed to sink, then at the end of 51 days, integrated P is about twice

what it is when either detritus or phytoplankton are allowed to sink at 1 m d^{-1}. Adding a moderate (0.01 Newton m^{-2}) positive alongbank wind stress, starting at day 30, increases the integrated phytoplankton stock by about 1%, while a stronger wind stress (0.05 Newton m^{-2}) increases the integrated phytoplankton stock by about 15%. This sense of wind stress creates coastal upwelling on the side of the bank under consideration, so it is not surprising that production is enhanced, although the modesty of the increase shows that transports associated with tidal mixing are more important.

Two cases, corresponding to runs 3 and 11 (Table 1) are selected for more careful consideration. Case 3 has relatively deep water over the bank (60–160 m) and relatively strong tidal currents, while case 11 has shallower water over the bank top (36–140 m) and weaker tidal currents. In case 3, the lateral mixing coefficient increases by about a factor of 2.5 when the flow is allowed to be three-dimensional, but in case 11, lateral mixing only increases by only about 30%. Thus, one would expect the biological impact of three-dimensionality (instability) to be greater in case 3 than 11.

Results at the end of the two-dimensional version of run 3 are shown in Figure 10, and summarized in Table 3. The nutrient concentrations are by far highest offshore of the tidal mixing front (around $x = 240$ km) and below about 20 m depth. Phytoplankton concentrations are highest in the well-mixed area ($x < 240$ km) and offshore in patches below about 20 m depth. A similar run, but that does not allow phytoplankton settling, has high phytoplankton concentrations throughout the upper 25 m. With sinking, almost no nutrient, phytoplankton, zooplankton or detritus is found near the surface in stratified waters: sinking plays a critical role in setting up the subsurface chlorophyll maximum in this model configuration. In all model runs, a pronounced maximum rate of nutrient uptake occurs on the mixed side of the front in the upper 10 m, and a much weaker tail extends along the thermocline on the stable side of the front. In this region, the "f-ratio" (the ratio of newly imported nutrient usage to total usage, computed as in Franks and Chen, 2001) is at a maximum: 0.88–0.92, depending on the run. Detritus and zooplankton concentrations are negligible (< 0.5 and < 0.005 m mole nitrogen m^{-3}, respectively) throughout 210 km $< x <$ 265 km. Results in the three-dimensional case at $y = 0$ km (Figure 11) are strikingly similar. Perhaps the main visual difference in the three-dimensional case is that the apparent width of the front (e.g., the distance between the 3 and 6 m mole nitrogen m^{-3} isopleths in Fig. 11a) varies considerably from section to section. This finding is not surprising in light of Figure 7, which shows substantial along-channel variations in frontal width and orientation. Another qualitative difference with the two-dimensional results is that, within the well-mixed zone, the phytoplankton concentrations appear to be more evenly distributed—less concentrated near the front—in the present three-dimensional calculations. It is worth noting however that climatological observations show that phytoplankton standing stock does not aggregate near the tidal mixing front, but is actually most concentrated near the Bank center (Thomas et al., 2003).

In both the two-and three-dimensional cases, there is a distinct and persistent tongue of high-phytoplankton water that extends from the front into the stratified water. The core of

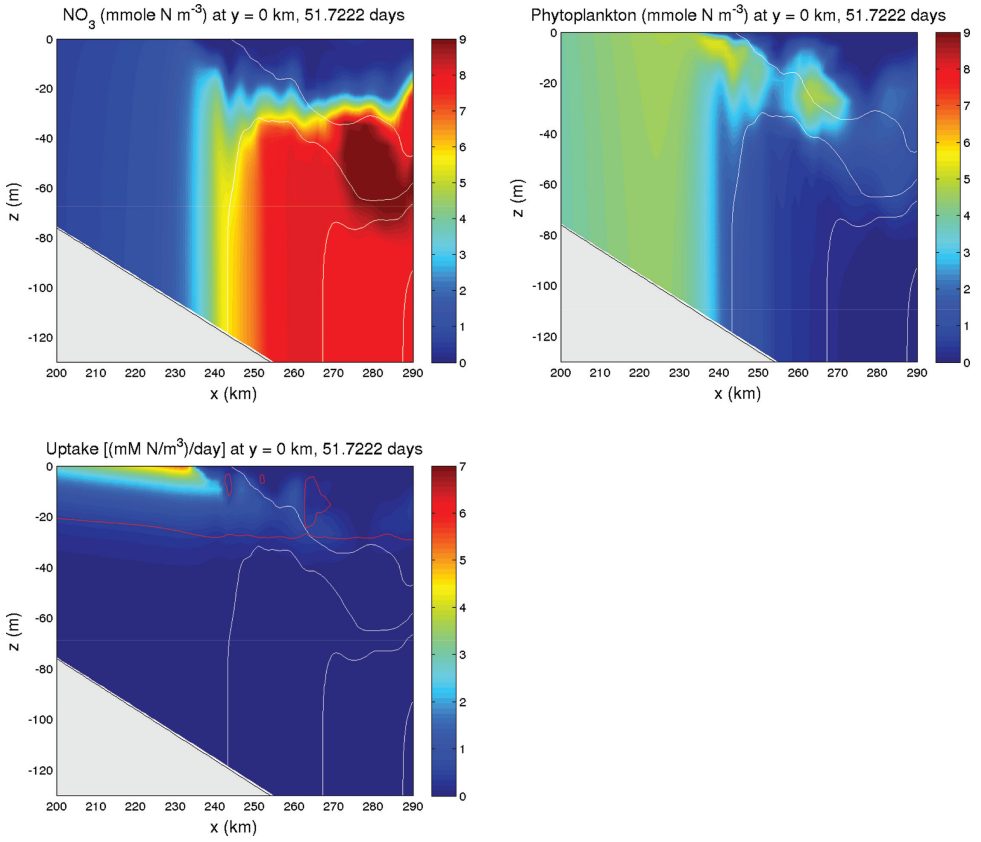

Figure 10. a) Nutrient concentration; b) phytoplankton concentration; and c) nutrient consumption (phytoplankton growth) for the two-dimensional version of model run 3 at day 51.7. Units for panels a and b are m mole nitrogen m^{-3}. Units in panel c are m mole nitrogen $(m^3\ day)^{-1}$. The red line in panel c is the depth at which phytoplankton growth is balanced by mortality and grazing.

Table 3. Results of NPZD model runs, integrated over $x = 210$–265 km, averaged over the last 20 model days.

Model	Average Phytoplankton Concentration (moles nitrogen m^{-2})	Average Nutrient Uptake (moles nitrogen $m^{-2}\ day^{-1}$)
3 (two-dimensional)	0.353	0.0347
3 (three-dimensional)	0.330	0.0315
11 (two-dimensional)	0.203	0.0203
11 (three-dimensional)	0.203	0.0201

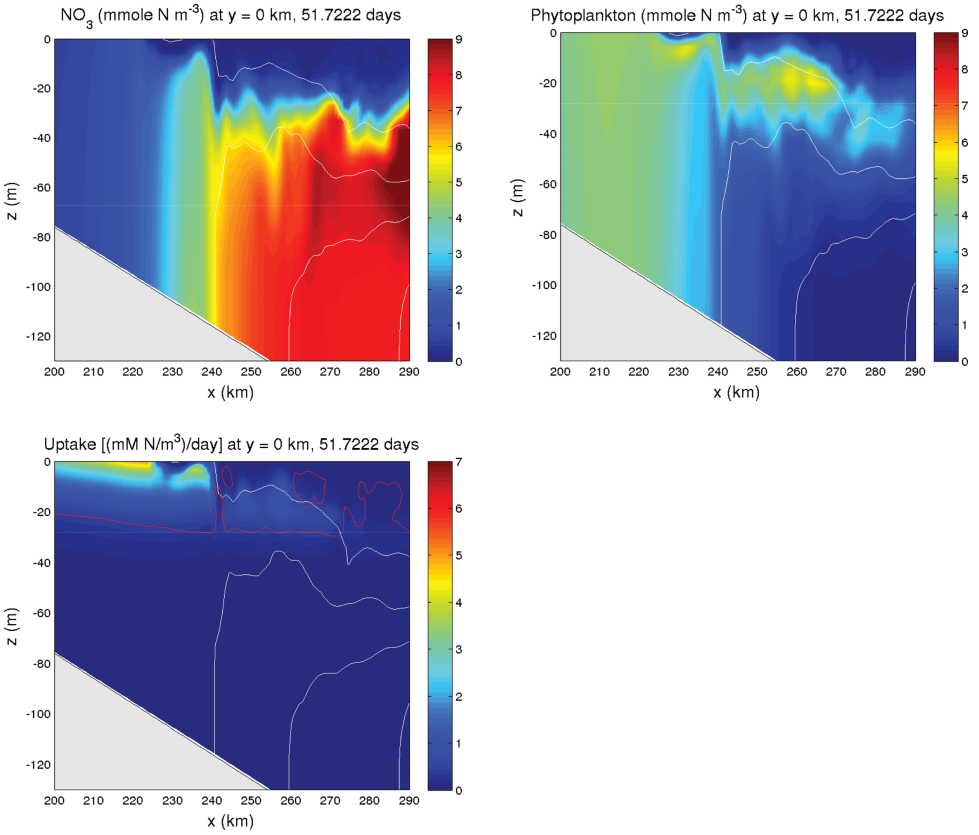

Figure 11. a) Nutrient concentration; b) phytoplankton concentration; and c) nutrient consumption (phytoplankton growth) for the three-dimensional version of model run 3 at day 51.7. Units for panels a and b are m mole nitrogen m^{-3}. Units in panel c are m mole nitrogen $(m^3\ day)^{-1}$. The red line in panel c is the depth at which phytoplankton growth is balanced by mortality and grazing.

this tongue lies above the nutricline and above the depth (typically about 28 m offshore of the front: see the red contour in Figs. 10c and 11c) where phytoplankton growth equals losses due to mortality and grazing. That is to say that some net growth occurs in this tongue. However, by far the largest growth is concentrated at the surface around 10–20 km inshore of the front. Analysis of the tongue shows that no single process accounts for its existence: vertical turbulent nutrient fluxes, *in situ* growth, phytoplankton mortality and lateral nutrient and phytoplankton mixing are all evidently important.

Comparing these particular two- and three-dimensional model runs (Table 3) leads to the tentative conclusion that allowing three-dimensional ("baroclinic") instabilities has surprisingly little impact. For case 11, when lateral mixing is only slightly enhanced, integrated biological activity (measured either as phytoplankton stock or as nutrient uptake)

changes by less than 1% between the two- and three-dimensional realizations. In case 3, where lateral mixing is greatly enhanced, the integrated phytoplankton stock declines by 7% and nutrient uptake declines by 10% as the flow becomes three-dimensional. Thus, for this particular choice of parameters, a substantially enhanced lateral mixing (case 3) leads to a mild decrease in phytoplankton growth and stock. It appears that the explanation is that the lateral eddy fluxes in the upper and lower parts of the water column tend to cancel. At depth, below the nutricline, eddy fluxes generally transport nutrients into the shallower, well-mixed region, but near the surface, eddy fluxes transport nutrient-depleted water from offshore into the well-mixed region. Indeed, for case 3, the depth integrated negative eddy nutrient flux (averaged over the last 38 tidal cycles - roughly 20 days) at the front is -1.87 m mole Nitrogen m^{-1} sec^{-1}, while the depth-integrated positive (offshore) nutrient flux is 1.68 m mole Nitrogen m^{-1} sec^{-1}: the fluxes cancel to within 11%. By comparison, for case 11 where baroclinic instability does not appreciably change the eddy coefficient, the integrated eddy nutrient fluxes cancel to within 37%. Similarly, for these two runs, the integrated positive and negative eddy heat fluxes cancel to within 9% for both runs. The conclusion here is that, although quasi-baroclinic instability enhances lateral mixing, the resulting enhanced shallow and deep eddy heat and nutrient fluxes tend to cancel. The nearly compensating lateral heat fluxes might help to explain why the very simple one-dimensional "h/u^3" reasoning (Simpson and Hunter, 1974) is so successful in rationalizing tidal mixing fronts.

6. Conclusions

The model configuration for all of the runs reported here was arranged so a tidal mixing front forms within a broad region with a uniform bottom slope. In the two-dimensional case, the bottom boundary layer appears to be subject to symmetric instabilities that play a substantial role in the cross-isobath exchange. In every case considered, the front is unstable to three-dimensional perturbations, and the primary energy source is generally baroclinic instability, although shear instabilities also contribute to varying degrees. The baroclinic instabilities occur in the presence of a fluctuating mean flow and of strong bottom frictional effects. That these instabilities exist is not surprising in light of previous idealized (e.g., van Heijst, 1986; Brink, 2012) or simulation (e.g., Badin et al., 2009) studies of this class of front. As might be expected, the three-dimensional instabilities lead to enhanced (relative to the two-dimensional case) lateral mixing, by up to around a factor of 6, and the degree of enhancement is closely related to the energy level of the baroclinic instability. Once the instabilities reach finite amplitude, their scale evolution is distinctly limited, and they do not undergo the sort of scale cascade that typifies idealized initial value problems (Brink, 2012). Unlike the initial value problem, the tidal mixing front meanders and is distorted, but it continues to exist. The front's survival and the lack of scale evolution are not surprising, of course, because the present problem, with its continual forcing and dissipation, is not free to evolve toward an equilibrium state.

Biological primary production is the ultimate motivation for this project: it seemed possible that enhanced lateral mixing would lead to an enhanced flux of nutrients into the well-mixed region. If this were true, the "tidal pumping" mechanism would be supplemented by eddy fluxes and so two-dimensional models, such as FC, would only provide a lower bound for the primary productivity in the well-mixed region. In order to test this idea, two NPZD model runs were executed for a) a case where three-dimensional eddy fluxes do not substantially enhance cross-frontal mixing (run 11), and b) a case where the enhancement is substantial (run 3). Only biological parameter values similar to FC's are treated. Not surprisingly, with little eddy enhancement, the two- and three-dimensional runs have similar levels of biological activity. In the case of where lateral mixing is more than doubled due to quasi-baroclinic instabilities, the biological activity (measured as either phytoplankton standing stock or as nutrient consumption) actually declines by 7–10% because of opposing fluxes in the upper and lower water column. Some caution should be exercised in treating this reduction as a general result, however, because the large potential parameter space associated with an NPZD model has not been explored. However, there is certainly no evidence here for the idea that the quasi-baroclinic instabilities enhance biological production.

One aspect of the observational record calls for comment. The extensive literature on tidal mixing fronts around the British Isles often includes evidence that these fronts are unstable (e.g., Simpson and James, 1986), and yet the comparably extensive literature on the analogous tidally mixed region on Georges Bank provides little insight on the subject: Garrett and Loder (1981) mention these instabilities in passing, and Chen et al. (2008) describe measurements and then simulate an observed frontal meander that could well be due to an instability. Why the contrast? One obvious comparison to consider is the expected energy levels of the frontal instabilities in both cases. In the Irish Sea, a typical summertime vertical temperature difference on the stable side of the front appears to be about 6.5 °C and the frontal depth is around 50 m (Simpson and James, 1986). On Georges Bank, a representative temperature difference would be around 3-4 °C and frontal depth about 50 m (Flagg, 1987). Result (16) suggests that the energy levels in the two cases would go as the ratio of $h_f^2 N^2$ assuming that c_D, $F(\omega)$ and s do not differ greatly between the two cases. The result is that frontal eddies in the Irish Sea ought to be about 1.6–3.2 times as energetic as would be found on Georges Bank. It thus seems possible that frontal eddies are less likely to be energetically important, hence observable, on Georges Bank than around the British Isles.

In the end, it appears that two-dimensional frontal models, such as that of FC, provide a very reasonable approximation to the processes governing nutrient supplies into a tidally mixed area. This conclusion, of course, does not rule out the possibility that frontal instabilities play an important role in exchange processes for properties other than nutrients.

Acknowledgments. Support from the National Science Foundation, Physical Oceanography program is gratefully acknowledged (Grant OCE-1059632). Comments from Deepak Cherian were also very helpful.

REFERENCES

Badin, G.; R.G. Williams; J.T. Holt and L.J. Fernand, 2009. Are mesoscale eddies in shelf seas formed by baroclinic instability of tidal fronts? J. Geophys. Res., *114*, C10021, doi:10.1029/2009JC005340.

Badin, G.; R.G. Williams and J. Sharples, 2010. Water-mass transformations in the shelf seas. J. Marine Res., *68*, 189–214.

Brink, K. H., 2012. Baroclinic instability of an idealized tidal mixing front. J. Marine Res., *70(4)*, 661–688.

Brink, K. H. and S. J. Lentz, 2010. Buoyancy Arrest and Bottom Ekman Transport: Part II, Oscillating Flow. Journal of Physical Oceanography, *40*, 636–655.

Chen, C.; Q. Xu; R. Houghton and R,C. Beardsley, 2008: A model-dye comparison experiment in the tidal missing front zone on the southern flank of Georges Bank. J. Geophys Res., *113(C2)*, doi:10.1029/2007JC003795.

Flagg, C. N., 1987. Hydrographic structure and variability. In: *Georges Bank*, R. H. Backus, editor, The MIT Press, Cambridge, Massachusetts, 108–124.

Franks, P.J.S. and C. Chen, 1996. Plankton production in tidal fronts: a model of Georges Bank in summer, J. Marine Res., *54*, 631–651.

Franks, P.J.S and C. Chen, 2001. A 3-D prognostic numerical model study of the Georges Bank ecosystem. Part II: biological-physical model. Deep-Sea Res. II, *48*, 457–482.

Garrett, C.J.R. and J.W. Loder, 1981. Dynamical aspects of shallow sea fronts. Phil. Trans. R. Soc. Lond. A., *302*, 563–581.

Haidvogel, D. B.; H. G. Arango; K. Hedstrom; A. Beckmann; P. Malanotte-Rizzoli and A. F. Shchepetkin, 2000: Model evaluation experiments in the North Atlantic Basin: Simulations in nonlinear terrain-following coordinates. Dyn. Atmos. Oceans, *32*, 239–281.

Hu, S.; D.W. Townsend; C. Chen; G. Cowles; R.C. Beardsley; R. Ji and R.W. Houghton, 2008. Tidal pumping and nutrient fluxes on Georges bank: a process-oriented modeling study. J. Marine Systems, *74*, 528–544.

James I.D., 1989: A three-dimensional model of circulation in a frontal region of the North Sea. *Dtsch. Hydrogr. Z.* 42, 231–247.

Loder, J.W., 1980. Topographic rectification of tidal currents on the sides of Georges Bank. J. Phys. Oceanogr., *10*, 1399–1416.

Loder, J.W.; K.F. Drinkwater; N.S. Oakey and E.P.W, Horne, 1993. Circulation, hydrographic structure and mixing at tidal fronts: the view from Georges Bank. Phil Trans.: Physical Sciences and Engineering, *343(1669)*, 447–460.

Loder, J.W. and D.G. Wright, 1985. Tidal rectification and frontal circulation on the sides of Georges Bank. J. Marine Res., *43*, 581–604.

O'Reilly, J.E.; C. Evans-Zetlin and D.A. Busch, 1987. Primary production. In Georges Bank (R.H. Backus, editor), the MIT Press, Cambridge, MA, 220–233.

Pasquet, A.; T. Szekely and Y. Morel, 2012. Production and dispersion of mixed waters in stratified coastal areas. Continental Shelf Research, 39–40, 49–77.

Shchepetkin, A.F. and J.C. McWilliams, 2005. The regional oceanic modeling system (ROMS): A split-explicit, free-surface, topography-following-coordinate oceanic model. Ocean Modelling, *9(4)*, 347–404.

Simpson, J.H. and J.R. Hunter, 1974. Fronts in the Irish Sea. Nature, *250*, 404–406.

Simpson, J.H. and I.D. James, 1986. Coastal and estuarine fronts. In Baroclinic Processes on Continental Shelves (C.N.K. Mooers, editor), American Geophysical Union, Washington D.C., 63–94.

Stone, P.H., 1966. On non-geostrophic baroclinic instability. J. Atmos. Sci., *123*, 390–400.

Thomas, A.C.; D.W. Townsend and R. Weatherbee, 2003. Satellite-measured phytoplankton variability in the Gulf of Maine. Continental Shelf Res., *23*, 971–989.

Thomas, P.J. and P.F. Linden, 1996. A laboratory model simulation of mixing across tidal fronts. J. Fluid Mech., *309*, 321–344.

van Heijst, G.J.F., 1986. On the dynamics of a tidal mixing front. In Marine Interfaces Ecohydrodynamics, (J.C.J. Nihoul, editor), Elsevier Oceanography Series, *42*, 165–194.

Wijesekera, H.W.; J.S. Allen and P. Newberger, 2003. A modeling study of turbulent mixing over the continental shelf: Comparison of turbulent closure schemes. J. Geophys. Res., *108(C3)*, 3103, doi:10.1029/2001JC001234.

Wright, D.G. and K.R. Thompson, 1983. Time-averaged forms of the nonlinear stress law. J. Phys. Oceanogr., *13(2)*, 341–345.

Young, W.R.; P.B. Rhines and C.J.R. Garrett, 1982. Shear-flow dispersion, internal waves ad horizontal mixing in the ocean. J. Phys. Oceanogr., *12(6)*, 515–527.

Received: *March 12, 2013*; revised: *June 24, 2013*.